Fabrication of CuO-based antireflection structures using self-arranged submicron SiO_2 spheres for thermoelectric solar generation

Tasuku Kondo[1], Mizue Mizoshiri[1]*, Masashi Mikami[2], Yoshitaka Itou[1], Junpei Sakurai[1], and Seiichi Hata[1]

[1] *Department of Micro-Nano Systems Engineering, Graduate School of Engineering, Nagoya University, Nagoya 464-8603, Japan*

[2] *National Institute of Advanced Industrial Science and Technology, Nagoya 463-8560 Japan*

E-mail: mizoshiri@mech.nagoya-u.ac.jp

We fabricated antireflection structures (ARSs) on the hot side of a thermoelectric generator (TEG) to absorb near-infrared (NIR) solar light with low reflective energy loss. First, the ARSs, composed of a CuO thin-film coated hemisphere array were designed using rigorous coupled wave analysis. Reflective loss was reduced to 6.7% at a grating period of 200 nm, as determined by simulation. Then, the ARSs were fabricated on a glass substrate using self-arranged submicron SiO_2 spheres, following the coating of a CuO thin film. Finally, the effect of the ARSs on NIR solar light generation was investigated by evaluating the generation properties of the TEG with the ARSs on the hot side. In comparison with the TEG with the CuO flat thin film on the hot side, the ARSs increased the temperature difference between the hot and cold sides by approximately 1.4 times. The CuO-based ARSs absorbed NIR solar light effectively.

1. Introduction

Solar light is a candidate for renewable energy. It can be converted to electric energy by two main methods, photovoltaic and thermoelectric conversions. Photovoltaic generators are commercially available. However, near-infrared (NIR) solar light, which is approximately 40% of the total solar energy, cannot be converted to electric energy using silicon photovoltaic modules. Moreover, the conversion efficiency decreases with increasing device temperature[1-2]. Recently, CIS solar cells, which convert solar light with a wide wavelength spectra (350–1300 nm), have been developed. The reduction in the conversion efficiency with increasing device temperature is also smaller than that absorbed in the silicon photovoltaic modules[3]. However, the solar energy that cannot be converted into electric energy becomes thermal energy. Thermoelectric generators (TEGs) convert thermal energy to electric energy, which reduces the dependence on solar light wavelength. TEGs convert the temperature difference, created between the hot and cold sides of pn junctions to electric energy. The generation voltage proportionally increases with the temperature difference and Seebeck coefficient of thermoelectric materials.

To improve efficiency of the conversion from solar energy to electric energy, thermal-photovoltaic hybrid generators have been studied[4-5]. The NIR solar light dispersed from the solar light has been used as thermal energy, which generated a temperature difference in the TEGs. We have also been developed a thermal-photovoltaic hybrid solar generator using thin-film TEGs[6]. The hybrid generator is composed of thin-film TEGs, a hot mirror, a focusing lens, and a photovoltaic solar panel. The NIR solar light was dispersed by the hot mirror and focused onto the hot side of the TEGs using the lens. The focused NIR light generated a temperature difference between the hot and cold sides of the pn junctions. However, the large volume of the lens and the large NIR focal length make it difficult to integrate and reduce the volume of the TEGs for NIR conversion.

Thin-film TEGs are classified into two by types of structure: a vertical type and a planar type. In the vertical type, the temperature difference is created in the thickness direction of the thermoelectric thin films[7-9]. On the other hand, in the planar type, the temperature difference is generated on the substrates of the thermoelectric thin films[10-16]. The planar type is advantageous because the temperature difference can be controlled by varying the length of the thermoelectric thin-film elements. However, the hot and cold sides

of the pn junctions are formed on the same plane, therefore necessitating the use of energy-focusing lenses for heating the hot sides[6]. If a large reflection difference on the hot and cold sides of the thermoelectric pn junctions is created, the temperature difference can be generated by irradiating solar light without the need for focusing lenses.

In this work, we designed and fabricated antireflection structures (ARSs) that absorb NIR solar light efficiently on the hot sides of TEGs for application in thermal-photovoltaic hybrid generators. ARSs are periodic structures with a subwavelength period. Many studies have focused on the design and fabrication of ARSs for application in optical devices such as camera lenses and photovoltaic solar panels to reduce the reflectance of available visible light[17-21]. First, we designed CuO-based ARSs using rigorous coupled wave analysis (RCWA) to decrease the energy loss of NIR solar light by taking account of the solar light spectra[22-24]. CuO exhibits higher reflectance and absorbance than SiO_2. To reduce the reflectance of CuO, a CuO absorber was formed as periodic structures with a subwavelength period. Then, we fabricated the ARSs on the hot sides on glass substrates using self-arranged submicron SiO_2 spheres and a CuO thin-film coating, which has excellent compatibility with the conventional microfabrication process[25-33]. SiO_2 spheres, which were monodispersed and have excellent sphericity, are easily arranged to form a monolayer. The monolayered spheres were more efficiently heated than the multilayered spheres owing to the low heat resistance. Finally, we investigated the effect of ARSs on NIR solar generation by setting the CuO-based ARSs on the hot side of a bulk thermoelectric module.

2. Procedure

2.1 Design concept of ARSs

ARSs with low NIR reflectance were designed. Figure 1 shows a schematic of the ARSs composed of a single layer of submicron SiO_2 spheres coated with a CuO thin film on a glass substrate. To date, various fabrication processes for ARSs have been reported such as electron beam lithography, two-beam interference, and self-arrangement of submicron spheres[25-33]. The self-arrangement of submicron spheres is an attractive method of fabricating ARSs in a relatively large area. In our study, the ARSs were formed on the hot sides of TEGs. In the future, the ARSs are expected to selectively form on the microsized hot sides of thin-film TEGs in a relatively large area. These fabrication methods using the

self-arrangement of submicron SiO_2 spheres and CuO thin-film deposition can be used with the fabrication of the microsized thin-film TEGs. Moreover, CuO thin films on the submicron SiO_2 spheres absorb NIR solar light. In comparison with other high-absorption materials such as carbon, CuO has a slightly lower absorbance of NIR solar light. However, it is difficult to deposit and pattern carbon thin films at a low temperature on the hot sides of TEGs because the melting points of Bi-Te and Sb-Te, which are excellent thermoelectric materials, are as lower as 585 and 617°C, respectively, which are lower than the carbon deposition temperature[34]. Carbon films are generally fabricated by chemical vapor deposition. The process temperature is as high as approximately 1000°C[35]. Therefore, the fabricated ARSs were expected to reduce their reflectance and absorb NIR efficiently.

2.2 Simulation method

Theoretical analysis of the reflectance of the ARSs is performed using RCWA (Grating Solver Development GSolver 5.2), which solves Maxwell's equations in a periodic structure using the coupled mode theory. The cross sections of the simulation models are shown in Fig. 2. By taking account of the absorption of CuO thin films of 300 nm film thickness, a periodic hemisphere model was used in the simulation. The energy loss by NIR solar light reflection on the ARSs was calculated using the simulation parameters shown in Table I. The database of refractive indices determined by the GSolver depended on the calculation wavelength. The periodic hemisphere was separated into 12 layers, which were enough for the simulation. The NIR solar light at 700−2500 nm was used for the simulation wavelength. The period and height of the hemisphere were varied from 100 to 800 nm and from 50 to 400 nm, respectively, because the ratio of the period to the height was fixed at 2:1. The NIR solar light was assumed to be irradiated with TE and TM mixed polarization to the ARSs. Therefore, the reflective energy loss on the ARSs was also assumed to be the average of the reflectances of TE and TM polarized lights. A diffraction order of ±10th was considered, which enabled us to eliminate the calculation loss. First, we calculated the maximal period to use the ARSs for the NIR solar light at 800–2500 nm wavelength. Then, we examined the dependence of reflectance on wavelength at the condition of various hemisphere periods. Finally, we optimized the period of the hemisphere ARSs to reduce the energy loss of the NIR solar light reflectance by taking account of the intensity distribution of the NIR solar

light.

2.3 Fabrication of ARSs

The ARSs were fabricated by arranging submicron SiO_2 spheres and a CuO thin film on a glass substrate of 200 μm thickness. The SiO_2 spheres were self-arranged to form a single layer by the dip-coating method. The accuracy of the withdrawal speed was 0.1 μm/s. The SiO_2 spheres were then dispersed in deionized water with the amphiphilic block copolymer F-127 as a dispersant using ultrasonic waves. The concentration ratio of SiO_2 spheres to deionized water to the amphiphilic block copolymer was 3:50:1. The glass substrate was dipped and withdrawn from the SiO_2 sphere mixed suspension. The withdrawal speed was varied from 1.0 to 100 μm/s to arrange the SiO_2 spheres into a single layer. The SiO_2 spheres were observed by scanning electron microscopy (SEM).

In addition, CuO thin films were deposited by the radio-frequency (RF) reactive magnetron sputtering method without substrate heating. A Cu sputtering target and Ar/O_2 mixed plasma were used for the film deposition. The purity, diameter, and thickness of the Cu target were 99.9%, 50.8 mm, and 5.0 mm, respectively. The distance between the target and the substrate when performing sputter deposition was 55 mm. The RF power and deposition pressure were 30 W and 1.0 Pa, respectively. The partial pressures of Ar and O_2 were 6:4, which were determined in reference to a study on CuO thin-film deposition by reactive magnetron sputtering[36].

2.4 Evaluation of the effect of ARSs

Figure 3 shows the evaluation setup for the ARSs. The effect of the ARSs on NIR solar light generation was evaluated using a bulk thermoelectric module. The open-circuit voltage of the thermoelectric module was 20.0 mV/K. The internal resistance of the module was 3.1 Ω. The glass substrate was fixed on the thermoelectric module using silicone paste, which has excellent thermal conductivity. Each ARS was 20 × 20 mm^2. The NIR solar light (> 800 nm wavelength) was separated from the solar light by a hot mirror that reflects only the NIR solar light. The NIR solar light was vertically irradiated to the ARSs. The thermoelectric module surface around the ARSs was covered with aluminum foil to reflect the solar light

without absorption. The generation voltage and power were evaluated by varying the load resistance. The sunlight power density was 81.5 mW/cm^2, which was measured as natural sunlight on a sunny day using a photodiode power meter (Thorlabs Inc., PM100D) calibrated at 632 nm wavelength.

3. Results and discussion

3.1 Simulation results

Figure 4 shows the reflectance of only the 0th order and the total reflectance of all the diffraction orders at wavelength from 700 nm to 2500 nm. The period was chosen to be 800 nm. The reflectance of only the 0th order and all the diffraction orders were almost the same over an 800 nm wavelength in both TE and TM polarized lights. The reflectances of the TE and TM polarized lights were 15.7 and 3.8%, respectively. These results indicate that diffraction light was eliminated from the reflection light under the condition that the period was smaller than the irradiated light wavelength. Consequently, the period of the ARSs was chosen to be less than 800 nm to reduce the reflectance of the NIR solar light to less than 800 nm wavelength.

The relationship between the reflectance and the wavelength is shown in Fig. 5. Figures 5(a) and 5(b) show the reflectances of the TM and TE polarized lights, respectively. The period of the ARSs was varied from 100 to 800 nm to eliminate the diffraction light of the NIR solar light in the wavelength range from 800 to 2500 nm wavelength. The reflectance depended on the wavelength and the period of the ARSs. The power of the solar light depends on its wavelength. To consider the intensity distribution of the solar light spectra for calculating the reflectance of the ARSs, the energy loss $l_A(\lambda)$ by the reflectance at a certain wavelength λ and a certain period A was described by the following equation:

$$l_A(\lambda) = r_A(\lambda) \cdot E(\lambda). \quad (1)$$

Here, the reflectance at a certain wavelength λ and a certain period A was defined as $r_A(\lambda)$. The solar energy at the wavelength λ was defined as $E(\lambda)$. Then, the total energy loss E_r by the reflected solar light at wavelengths from 800 to 2500 nm is described using the following equation:

$$E_r = \int_{\lambda=800nm}^{\lambda=2500nm} l_A(\lambda). \quad (2)$$

Finally, the energy loss rate of the solar light, L_A, was expressed using the total solar energy at wavelengths from 800 to 2500 nm, E_T, as follows:

$$L_A = {E_r}/{E_T} . \quad (3)$$

Both TM and TE polarized light reflectances were calculated using Eq. (3). In general, the ratio of TM polarized light to TE polarized light depends on the incident angle of the solar light. In this analysis, we assumed that the incident light was vertically irradiated to the ARSs. Therefore, the average of the reflectances of TM and TE polarized lights was used for the reflectance of the NIR solar light.

Figure 6 shows the dependence of the energy loss on the period of CuO ARSs. The energy loss changed with the grating period. When the grating period was 200 nm, the energy loss exhibited a minimum value of 6.7%. The energy loss of the CuO thin film was 20.4%, so this result shows that ARSs can reduce energy loss. By taking account of the results, the ARSs were designed to have periodic hemisphere structures with a period of 200 nm.

3.2 Fabrication result of ARSs

The ARSs were fabricated using self-arranged SiO_2 spheres and a CuO thin film coating. The diameter of the SiO_2 spheres used was 200 nm. Figure 7 shows the SEM images of the arranged SiO_2 spheres. The withdrawal speeds in Figs. 7(a)−7(d) are 50, 10, 2, and 1 μm/s, respectively. When the withdrawal speed was higher, as shown in Figs. 7(a) and 7(b), the glass substrates were observed. On the other hand, when the withdrawal speed was lower, as shown in Fig. 7(d), the multilayered SiO_2 spheres were arranged. The single-layered SiO_2 spheres were arranged on the glass substrate at a withdrawal speed of 2 μm/s. SiO_2 spheres were self-arranged on the substrate with a single layer for the fabrication of the ARSs. A CuO thin film of 300 nm thickness was coated onto the arranged SiO_2 spheres by RF reactive magnetron sputtering.

3.3 Evaluation of the effect of ARSs

The effect of the ARSs on NIR solar light generation was evaluated by the irradiation of the NIR solar light. Figures 8(a) and 8(b) show the generation voltage and power with varying load resistance, respectively. The generation voltage of the thermoelectric module with the ARSs was larger than that of the module with the CuO flat thin film (without the ARSs). The

open-circuit voltages of the bulk thermoelectric module with and without the ARSs were 6.72 and 5.07 mV, respectively. The temperature difference between the hot and cold sides of the thermoelectric pn junctions was estimated to be 0.34 and 0.25°C, respectively, by taking account of the open-circuit voltage of the thermoelectric module, i.e., 20 mV/K. It indicates that the ARSs increased thier absorption of the NIR solar light by reducing the reflectance, resulting in a temperature difference approximately 1.4 times that of the CuO flat thin film. The maximum outputs of the module with the ARSs and CuO flat thin film (without the ARSs) were 3.81 and 2.05 mW, respectively. The maximum power of the module with the ARSs became approximately 1.8 times that of the module without the ARSs. We formed that the ARSs fabricated on the hot sides enhanced their thermoelectric generation by improving NIR solar light absorption.

4. Conclusions

We designed ARSs, which are composed of self-arranged SiO_2 spheres and a CuO thin-film coating, using RCWA. The minimum energy loss was 6.7% when the grating period was 200 nm as determined by simulation. The ARSs were fabricated using the self-arrangement of SiO_2 spheres by dip-coating, following CuO thin-film deposition. The effect of the ARSs on NIR solar light was investigated using a bulk thermoelectric module. The temperature difference of the thermoelectric module with the ARSs increased by approximately 1.4 times. We revealed that the ARSs fabricated on the hot side of the TEG enhanced their thermoelectric generation by improving NIR solar light absorption.

Acknowledgments

This study was partially supported by the Nanotechnology Platform Program (Micro-Nano Fabrication) of the Ministry of Education, Culture, Sports, Science and Technology, Japan (MEXT).

References

1) E. Skoplaki and J. A. Palyvos, Sol. Energy **83**, 614 (2009).
2) B. Rech and H. Wanger, Appl. Phys. A **69**, 155 (1999).
3) I. Konovalov, Thin Solid Films **451**, 413 (2004).
4) N. Wang, L. Han, H. He, N. Park, and K. Koumoto, Energy Environ. Sci. **92**, 367 (2011).
5) M. Mizoshri, M. Mikami, K. Ozaki, and K. Kobayashi, Jpn. J. Electron. Mater. **41**, 1713 (2012).
6) M. Mizoshri, M. Mikami, and K. Ozaki, J. Appl. Phys. **51**, 06FL07 (2012).
7) G. J. Snyder, J. R. Lin, C. Huang, and J. P. Fleurial, Nat. Mater. **2**, 528 (2003).
8) Z. Wang, V. Leonov, P. Fiorini, and C. V. Hoof, Sens. Actuators A **156**, 95 (2008).
9) K. H. Lee and O. J. Kim, Int. J. Heat Mass Transfer **50**, 1982 (2007).
10) J. Weber, K. Potje-Kamloth, F. Hasse, P. Detemple, F. Volklein, and T. Doll, Sens. Actuators A **132** 325 (2006).
11) P. Li, L. Cai, P. Zhai, X. Tang, Q. Zhang, and M. Niino, J. Electron. Mater. **39**, 1522 (2010).
12) D. Kraemer, B. Poudel, H.-P. Feng, J. C. Caylor, B. Yu, X. Yan, Y. Ma, X. Wang, D. Wang, A. Muto, K. McEnaney, M. Chiesa, Z. Ren, and G. Chen, Nat. Mater. **10** 532 (2011).
13) R. Amatya and R. J. Ram, J. Electron. Mater. **39** 1735 (2010).
14) M. Takahashi, T. Shirakawa, K. Miyazaki, and H. Tsukamoto, Sens. Actuators A **138**, 329 (2007).
15) J. Su, V. Leonov, M. Goedbloed, Y. V. Andel, M. C. D. Nooijer, R. Elflink, Z. Wang, and R. J. M. Vullers, J. Micromech. Microeng. **20**, 104005 (2010).
16) S. M. Yang, T. Lee, and M. Cong, Sens. Actuators A **157**, 258 (2010).
17) C. K. Huang, K.W. Sun, and W. L. Chang, Opt. Express **20**, A85 (2012).
18) W. Joo, H. J. Kim, and J. K. Kim, Langmuir **26**, 5110 (2010).
19) S. Chattopadlhyay, Y. F. Huang, Y. J. Jen, A. Guangly, K. H. Chen, and L. C. Chen, Mater. Sci. Eng. **69**, 1 (2010).
20) J. Y. Chen, W. L. Chang, C. K. Huang, and K. W. Sun, Opt. Express **19**, 14411 (2011).
21) M. Y. Chiu, C. H. Chang, M. A. Tsai, F. Y. Chang, and P. Yu, Opt. Express **18**, A308 (2010).
22) S. L. Jaiswal, J. T. Simpson, S. P. Withrow, C. W. White, and P. M. Norris, Appl. Phys. A **77**, 57 (2003).
23) S. Zhang, W. Fan, N. C. Panoiu, K. J. Malloy, R. M. Osgood, and S. R. J. Brueck, Phys.

Rev. Lett. **95**, 137404 (2005).

24) K. C. Sahoo, Y. Li, and E. Y. Chang, Comput. Phys. **180**, 1721 (2009).
25) T. Yanagishita, K. Nishio, and H. Masuda, Appl. Phys. Express **2**, 022001 (2009).
26) B. J. Bae, S. H. Hong, E. J. Hong, H. Lee, and G. Y. Jung, Jpn. J. Appl. Phys. **48**, 1R (2009).
27) Y. Xia, Y. Yin, Y. Lu, and J. MacLellan, Adv. Funct. Mater. **13**, 907 (2003).
28) Y. Yin, Y. Yu, B. Gates, and Y. Xia, J. Am. Chem. Soc. **123**, 8718 (2001).
29) H. L. Chen, S. Y. Chuang, C. H. Lin, and Y. H. Lin, Opt. Express **15**, 14793 (2007).
30) K. S. Han, H. Lee, D. Kim, and H. Lee Sol. Energy Mater. Sol. Cells **93**, 1214 (2009).
31) S. Zhou, T. Sakamoto, J. Wang, A. Sugawara-Narutaki, A. Shimojima, and T. Okubo, Langmuir **28**, 13181 (2012).
32) K. Akimoto, S. Ishizuka, M. Yanagita, Y. Nawa, G. K. Paul, and T. Sakurai, Sol. Energy Mater. **80**, 715 (2006).
33) S. Ishizuka, T. Maruyama, and K. Akimoto, J. Appl. Phys. **39**, L786 (2000).
34) N. Peranio, M. Winkler, A. Aabdin, J. Kőnig, H. Bőttner, and O. Eibl, Phys. Status Solidi A **209** 289 (2012).
35) A. M. Cassell, J. A. Raymakers, J. Kong, and H. Dai, J. Phys. Chem. 109, 6484 (1999).
36) J. F. Pierson, A. Thobor-Keck, and A. Billard, Appl. Surf. Sci. **210**, 359 (2003).

Figure Captions

Fig. 1. Schematic illustration of the ARSs on a glass substrate.

Fig. 2. Cross section of a periodic hemisphere model for ARSs.

Fig. 3. Schematic of the evaluation setup of the effect of ARSs on TEG.

Fig. 4. Reflectances of 0th order and total of all diffraction orders at wavelength from 700 to 1300 nm at the grating period of 800 nm.

Fig. 5. Reflectances of the (a) TM and (b) TE polarized solar lights.

Fig. 6. Dependence of energy loss on the period of the CuO ARSs.

Fig. 7. SEM images of the self-arranged submicron SiO_2 spheres at the withdrawal speeds of (a) 50, (b) 30, (c) 2.0, and (d) 1.0 μm/s.

Fig. 8. I-V and I-P properties of the TEGs with and without the ARSs.

Table I.

Simulation parameters.

Refractive index (air) at 800 nm	1
Refractive index (Cu) at 800 nm	0.32+*j*6.58
Refractive index (CuO) at 800 nm	2.65+*j*0.009
Incident light wavelength (nm)	700–2500
Incident angle (deg)	0
Period (nm)	100–800
Height (nm)	50–400
Diffraction order	±10
Layer number	12

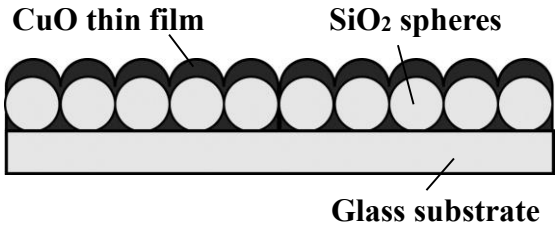

Fig. 1.

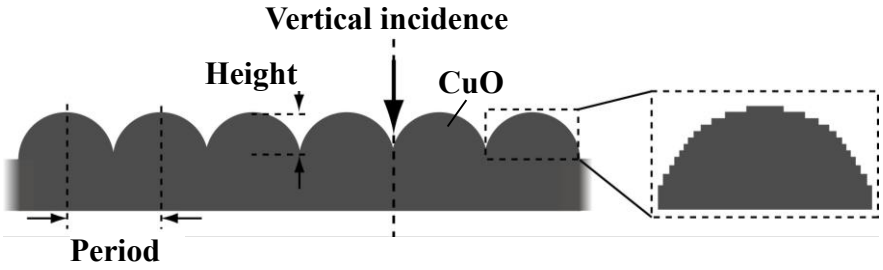

Fig. 2.

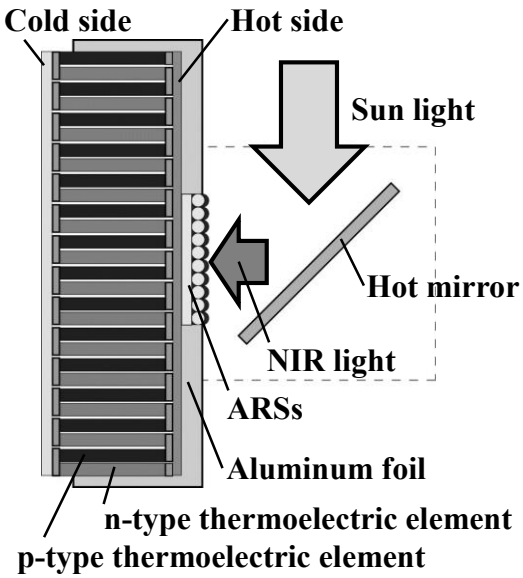
Cold side
Hot side
Sun light
Hot mirror
NIR light
ARSs
Aluminum foil
n-type thermoelectric element
p-type thermoelectric element

Fig. 3.

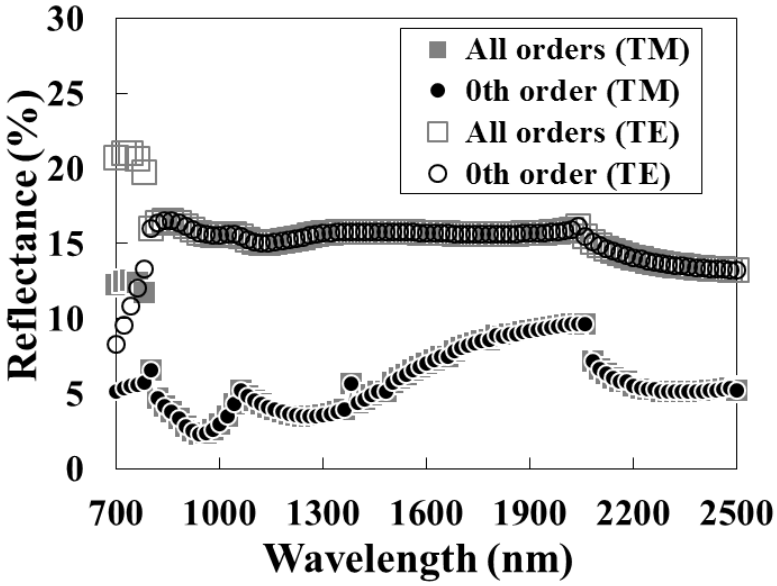
All orders (TM)
0th order (TM)
All orders (TE)
0th order (TE)
Reflectance (%)
30
25
20
15
10
5
0
700
1000
1300
1600
1900
2200
2500
Wavelength (nm)

Fig. 4.

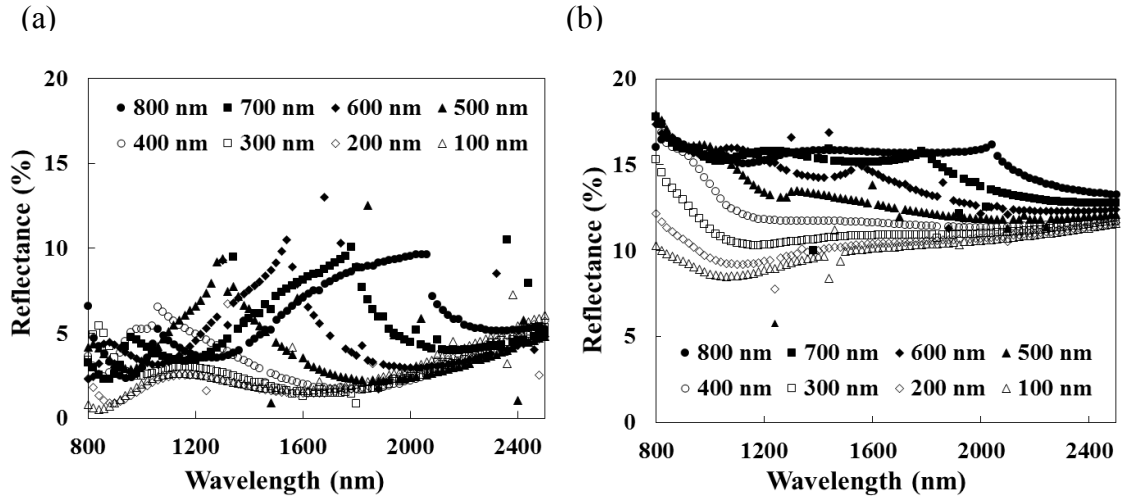
(a)
(b)
Reflectance (%)
Wavelength (nm)
800 nm
700 nm
600 nm
500 nm
400 nm
300 nm
200 nm
100 nm
0
5
10
15
20
800
1200
1600
2000
2400

Fig. 5.

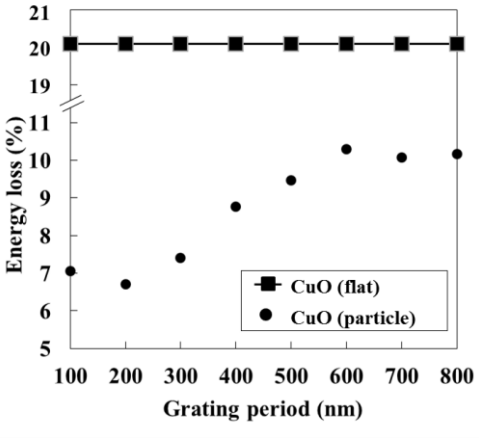
21
20
19
11
10
9
8
7
6
5
Energy loss (%)
100
200
300
400
500
600
700
800
Grating period (nm)
CuO (flat)
CuO (particle)

Fig. 6.

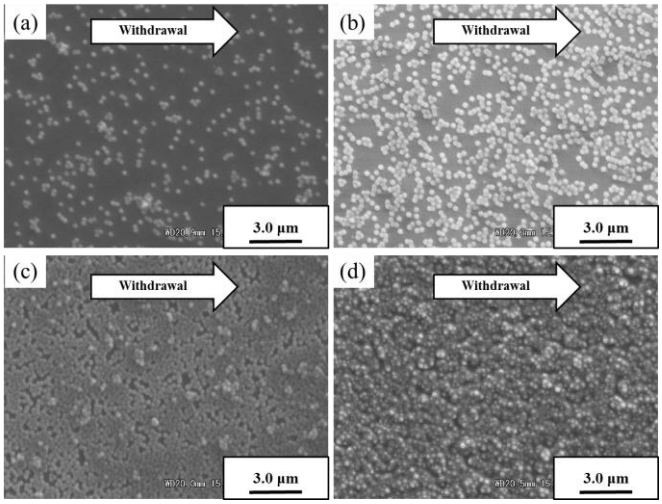
(a)
Withdrawal
3.0 μm
(b)
Withdrawal
3.0 μm
(c)
Withdrawal
3.0 μm
(d)
Withdrawal
3.0 μm

Fig. 7.

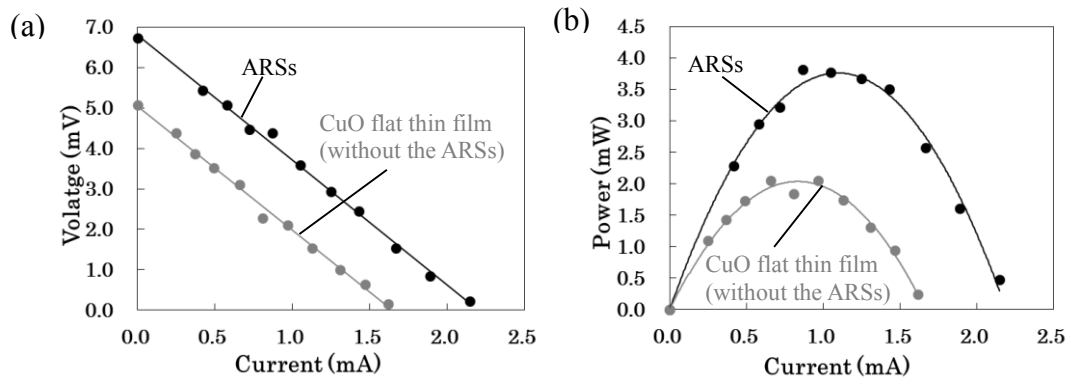
(a)
Volatge (mV)
Current (mA)
ARSs
CuO flat thin film
(without the ARSs)
(b)
Power (mW)
Current (mA)
ARSs
CuO flat thin film
(without the ARSs)

Fig. 8.